Hindawi
Advances in Civil Engineering
Volume 2024, Article ID 3659021, 18 pages
https://doi.org/10.1155/2024/3659021

Research Article

The Effect of Excavation Disturbance on the Stability of Bedding Cataclastic Rock Mass High Slope Containing Multimuddy Interlayers

Fei Liu,[1] **Jiaming Zhang**,[1] **Pengzheng Guo**,[1] **Wenlian Liu**,[2] **Zhiqiang Wang**,[2] **and Jipu Chen**[1]

[1]*Faculty of Civil Engineering and Mechanics, Kunming University of Science and Technology, Kunming 650504, China*
[2]*Kunming Prospecting Design Institute of China Nonferrous Metals Industry Co. Ltd., Kunming 650051, China*

Correspondence should be addressed to Jiaming Zhang; zhangjiaming@kust.edu.cn

Received 3 September 2023; Revised 2 January 2024; Accepted 9 February 2024; Published 21 February 2024

Academic Editor: Nicola Buratti

In China, slope engineering occasionally faces landslides in rocky slopes containing muddy interlayers, primarily triggered by excavation activities. These incidents lead to considerable human casualties and substantial economic losses. However, existing studies predominantly concentrate on the excavation-induced impacts on the stability of rocky slopes characterized by single-layered soft and weak interlayers. Conversely, reports on how excavation influences the stability of bedding cataclastic rock mass high slope containing multimuddy interlayers remain notably absent in the literature. Moreover, unloading due to excavation can swiftly compromise the mechanical integrity and overall quality of the rock mass, consequently impacting the stability of slopes postexcavation. Therefore, this paper modeled the unstable slope excavated at a waste incineration power plant in Yuxi, Yunnan, using the finite element strength reduction method. This approach was employed to comprehensively simulate the entire process of artificial multilevel excavation in a bedding cataclastic rock mass high slope containing multimuddy interlayers. This study investigated the impact of multilevel artificial excavation on slope stability by thoroughly considering factors including alterations in slope morphology, unloading effects, and the degradation of geotechnical parameters. The research yielded the subsequent conclusions. Multimuddy interlayers were the key to the slope's instability. For slopes subjected to such multilevel excavation, efforts were made to minimize the exposure of muddy interlayers. Slopes above exposed muddy interlayers did not require additional support, while those below needed prioritized reinforcement. The likely instability mode of the actual slope was local destabilization leading to landslides. Furthermore, when using numerical simulation methods to study the impact of excavation disturbances on the stability of such slopes, it was necessary to consider the deterioration of geotechnical parameters to obtain results more reflective of actual conditions. These research findings provided valuable theoretical and empirical support for studies on similar excavated slopes.

1. Introduction

The western region of China has complex geological conditions, with a significant number of bedding cataclastic rock mass high slope containing multimuddy interlayers [1–6]. The ongoing construction of major projects, such as the Sichuan–Tibet Railway, Yunnan–Tibet Railway, Central Yunnan Water Diversion Project, and the Western Development Strategy, only exacerbates potential stability issues of these excavated slopes. The region where the rock mass is damaged by excavation is a common phenomenon in engineering geology [7–9]. Excavation, accompanied by the deformation of the rock mass during the unloading process, leads to a decline in rock mass quality, significantly impacting the safety and stability of slope geotechnical engineering [10]. After excavation disturbance disrupted the slope's original stability, the slope became highly prone to sliding along its various muddy interlayers. This form of failure is more complex compared to slopes without or with only a single muddy interlayer. In some

cases, instability and collapse of these slopes may result in severe casualties and significant economic losses.

Currently, research on excavated slopes containing muddy interlayers involves multiple aspects. Researchers have employed various methods, including case analysis, mathematical analysis, physical modeling, and numerical simulation. Wang reported four typical landslide cases of slopes with muddy interlayers in Guizhou. The author proposed that the primary conditions for the instability of slopes with muddy interlayers are twofold: excavation leading to the exposure of muddy interlayers on the slope face and upper layer soil detachment, with rainwater infiltration causing softening and reduced shear strength of the muddy interlayers [11]. Su et al. [12] derived the differential equations for the progressive failure of bedding rock mass slopes containing muddy interlayers and theoretically analyzed the process and stages of progressive failure. Mu et al. [13] conducted model experiments to visually depict the deformation and failure evolution process of a high slope containing muddy interlayers in a site excavation in Southern Guizhou under different working conditions. However, when designing models for experiments, researchers need to choose larger dimensions to minimize the influence of size effects. Therefore, model experiments are not suitable for simulating large-scale engineering projects.

In contrast, numerical simulation methods are more economical and better suited for capturing the complexity of real engineering projects. They are particularly suitable for addressing large and intricate engineering issues [14, 15]. Chen et al. [16] and Yun et al. [17] conducted numerical simulations of excavation support for slopes containing single-layer weak interbeds to optimize their construction schemes. Fan utilized MatDEM simulation to model the process of distributed slope excavation. The study indicated that the presence of weak interlayers has a substantial impact on the stability of slope excavation [18]. Chai [19] used RFPA software to simulate the step-by-step excavation process of slopes containing weak interlayers. The study pointed out that excavation-induced unloading is the most significant influencing factor on slopes with weak interlayers [19]. Xue et al. [20] conducted numerical simulations based on a basalt landslide with inclined weak interlayers. They analyzed the stability of the slope before and after excavation and proposed that the main cause of rockslide is the presence of excavation and inclined weak interlayers [20].

Upon reviewing the aforementioned literature, it was found that most of the related studies focused on general rock slopes with muddy interlayers, emphasizing the impact of excavation on changing slope morphology and the effects of unloading on slope stability. Research on bedding cataclastic rock mass slopes containing multimuddy interlayers has not yet been reported. Excavation not only alters the slope morphology but also, through unloading, redistributes the stress in the surrounding rock mass near the excavation face. This results in the formation of an excavation-disturbed zone, leading to rapid degradation of the mechanical characteristics and quality of the rock mass [21, 22]. The impact of artificial grading excavation on the stability of bedding cataclastic rock mass high slopes containing multimuddy interlayers can fill the research gap in the study of muddy interlayers, offering a substantial reference for further investigation. Therefore, this case study was based on the unstable high slope of a waste incineration power plant in Yuxi and employed finite element analysis to examine the impact of artificial multilevel excavation on slope stability, considering factors such as support and the deterioration of geotechnical parameters. The analysis results can provide useful references for similar slope engineering projects.

2. Geological Settings

A waste incineration power plant in Yunnan is located on the Shiliuying Slope at the southern edge of the Yuxi Basin in Yunnan, China. The excavation site formed a high bedding cut slope with a length of 244 m and a height of 42.5 m (Figure 1(a)). During the excavation construction process, the slope experienced multiple instances of instability (Figures 1(b) and 1(c)). The slope features developed fracture structures, with the lithology being the Ediacaran Doushantuo dolomite. The dolomite contains multimuddy interlayers (Figure 1(d)), with the rock strata having a dip direction of 195° and a dip angle of 22°. The dolomite rock mass is fragmented, with rock quality designation (RQD) values ranging between 0% and 10%. The basic quality grade of the rock mass is between IV and V. The integrity of the rock mass should be considered fragmented to extremely fragmented. The thickness of the muddy interlayers ranges between 1 and 25 mm, with spacings varying from 3.7 to 49.1 cm.

3. Methods

3.1. Calculation Model and Parameter Selection. A section close to the axis of the landslide, with a significant height and passing through the main sliding surface, was selected for modeling and calculation. Based on the preliminary geological exploration data, the DE segment of the slope support section was chosen to establish a numerical model, named "Model I" (Figure 2).

The DE section excavation formed four levels of slopes. The first level had an elevation between 1,831 and 1,841 m with a slope ratio of 1 : 0.5. The second level's elevation ranged from 1,841 to 1,851 m with the same slope ratio of 1 : 0.5. The third level was between 1,851 and 1,861 m with a slope ratio of 1 : 0.75. The fourth level ranged from 1,861 to 1,873.5 m with a slope ratio of 1 : 1. Platforms were set between the slopes, and the widths of all three platforms were 2 m each. The slope height H of section DE was 40.5 m. Based on the research findings on the accuracy of slope stability safety factor calculations by Zhang et al. [23], a 2D calculation model was determined as shown in Figure 1. The model was 237.7 m wide. The elevation of the left boundary ranged from 1,791 to 1,894.9 m with a height of 103.9 m, while the elevation of the right boundary ranged between 1,791 and 1,831 m, with a height of 40 m.

The boundary conditions for the calculation model were set as follows: The bottom boundary of the slope was a fixed constraint, the left and right boundaries were normal constraints, and the ground surface of the slope was a free

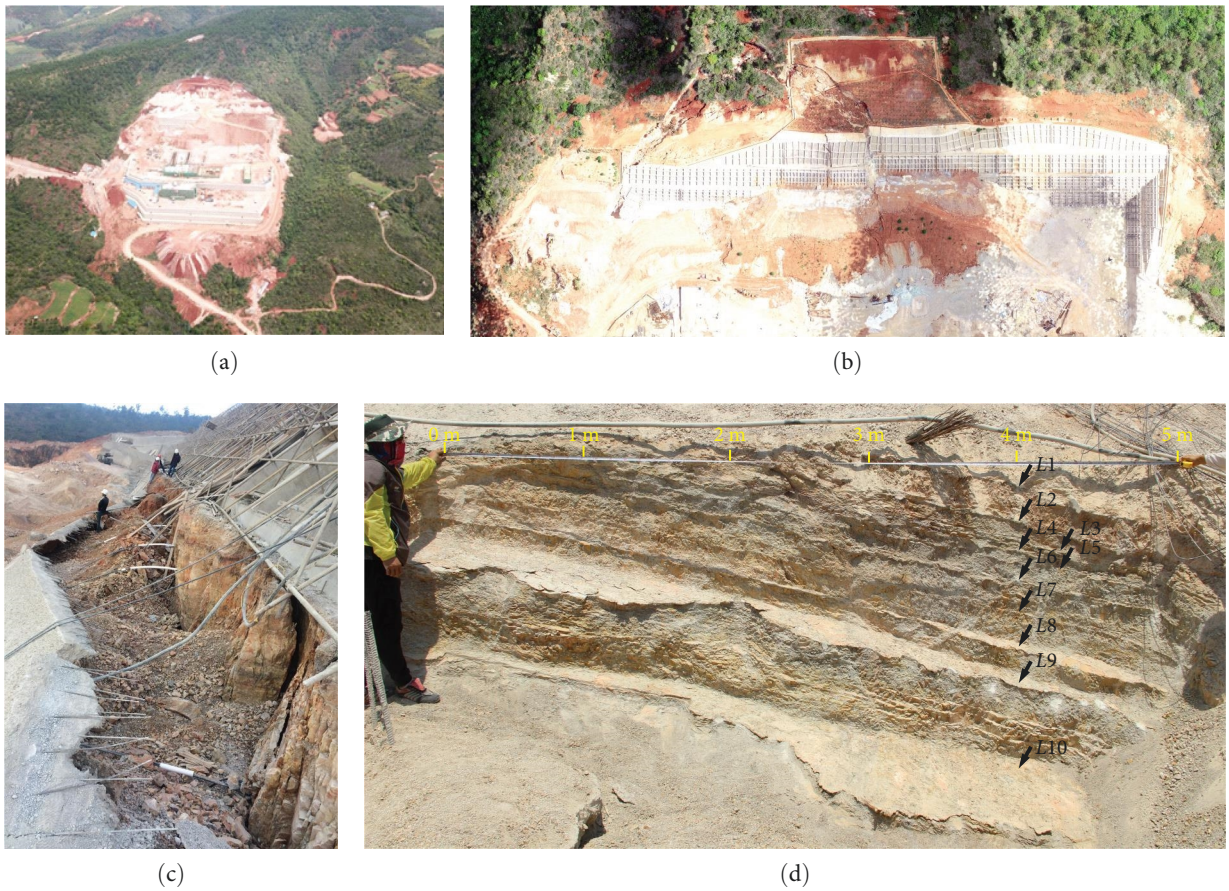

Figure 1: Engineering area situation map. (a) Engineering site topography and geomorphology. (b) Central slope instability. (c) Partial collapse of slope. (d) Profile at observation point and distribution of muddy interlayers.

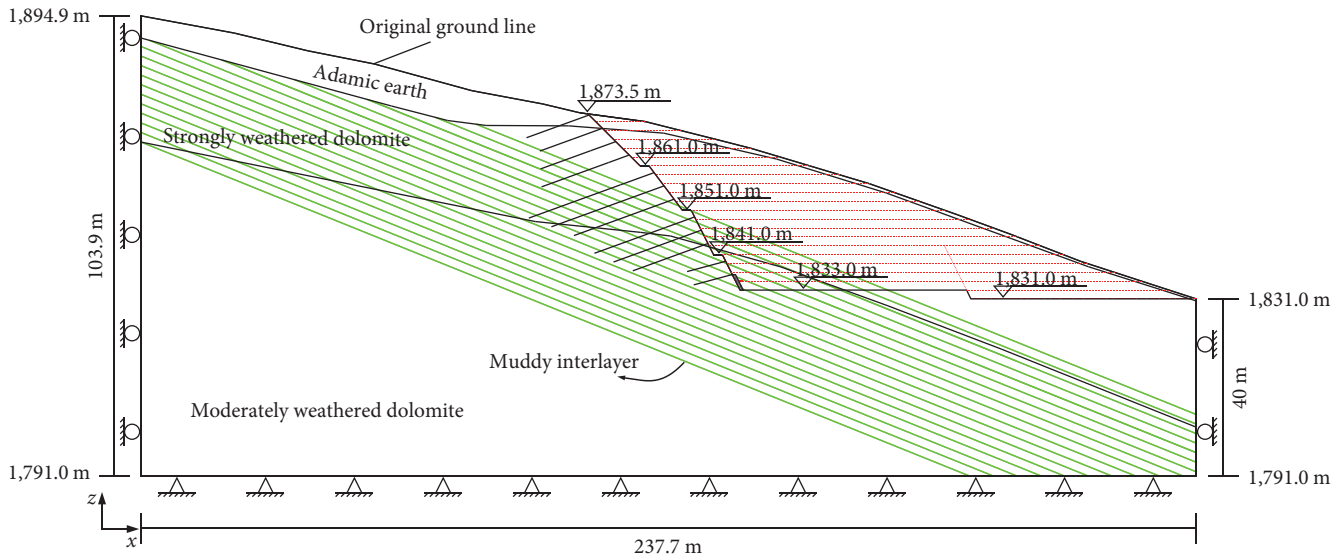

Figure 2: Model I—slope support profile of section DE.

boundary. The calculation model consists of cataclastic rock mass and muddy interlayers. The calculation model consisted of cataclastic rock mass and muddy interlayers within the geotechnical body. To avoid computational distortion and maintain accuracy, both the cataclastic rock mass and muddy interlayers were simulated using solid elements. The cataclastic rock mass and the muddy interlayers were considered as ideal elastic-to-plastic materials, with the

Table 1: Initial physicomechanical parameters of geotechnical bodies.

Geotechnical type	Density (g/cm^3)	Modulus of elasticity (MPa)	Poisson's ratio	Cohesion (MPa)	Internal friction angle (degree)
Adamic earth	1.75	300	0.35	0.0578	13.8
Strongly weathered dolomite	1.90	300	0.30	0.08	30
Moderately weathered dolomite	2.50	500	0.25	0.1	35
Muddy interlayer	2.73	20	0.35	0.03	16

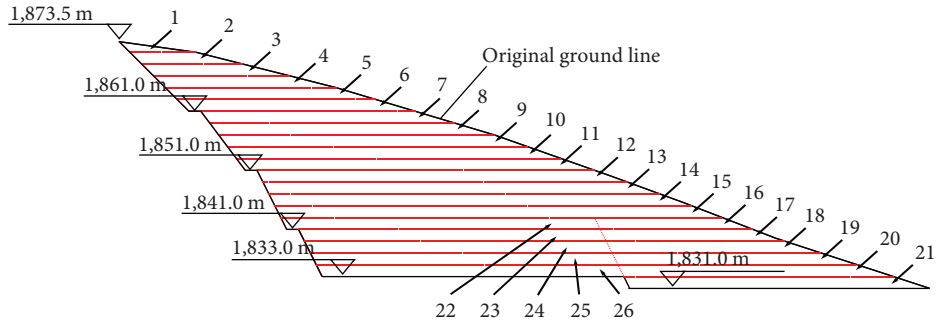

Figure 3: Model I—steps for excavation of slopes, level by level.

Table 2: Lattice girder: simulation parameters for plate elements.

Material type	Modulus of elasticity (MPa)	Equivalent thickness (m)	Volumetric weight (kN/m^3)	Axial stiffness (kN)	Bending stiffness (kN·m^2)	Poisson's ratio
Resilient	3×10^4	0.204	5.1	6.12×10^6	2.122×10^4	0.15

yield criterion for both adhering to the traditional Mohr–Coulomb model [24]. The Mohr–Coulomb criterion could be expressed using the invariants I_1, J_2, and θ_σ, as shown in Equation (1).

$$\frac{1}{3}I_1\sin\varphi+\left(\cos\theta_\sigma-\frac{1}{\sqrt{3}}\sin\theta_\sigma\sin\varphi\right)\sqrt{J_2}-\cos\varphi=0, \tag{1}$$

where I_1 represents the first invariant of the stress tensor, J_2 represents the second invariant of the stress deviator tensor, and θ_σ represents the stress Lode angle.

Finite element numerical simulations were performed using the geotechnical engineering software PLAXIS 2D 2020, without accounting for the impact of pore water pressure and while neglecting the dilation angle ($\psi=0$). In other words, a nonassociated flow law was employed, resulting in conservative calculation results [23]. The cataclastic rock mass parameters can be found in Table 1.

The spacing of the muddy interlayers ranged from 3.7 to 49.1 cm, with an average of 20.4 ± 12.0 cm. Zhang et al. [25] had shown that the overall stability safety factor of a slope decreased as the number of muddy interlayers increased (with reduced spacing). The decisive influence on the slope's safety factor was the muddy interlayer passing through the toe of the slope. Therefore, the muddy interlayers in the calculation model were set as follows: with an inclination of 22°, a spacing of 2 m, and a thickness of 0.05 m.

Based on the actual engineering conditions, the excavation steps are shown in Figure 3. The excavation procedure for Model I consists of 26 steps.

Based on the geotechnical engineering survey report, the physical and mechanical parameters of the rock and soil mass were determined [26]. The calculated parameters are presented in Table 1. The slope was comprehensively stabilized using rock bolt support, cable-braced lattice beam support, slope shotcrete, mortared stone gravity retaining walls, and drainage measures (Figure 2). The rock bolts were modeled using embedded pile elements, with a borehole diameter of 0.15 m and a pile element spacing of 3 m.

The lattice beams were simulated using plate elements, with simulation parameters detailed in Table 2. The elastic modulus of C30 concrete was 3×10^4 MPa. The longitudinal and transverse spacing of the lattice beams were both set at 3 m, with a cross-sectional dimension of 0.4×0.4 m. Following the stiffness equivalence principle, the lattice beams were equivalently represented as plates:

$$\frac{a\times a^3}{12}=\frac{l\times h^3}{12}. \tag{2}$$

Table 3: Physical and mechanical parameters of slurry block stone gravity retaining wall.

Material type	Volumetric weight (kN/m^3)	Modulus of elasticity (MPa)	Poisson's ratio
Resilient	22	2.3×10^4	0.18

Table 4: Physical and mechanical parameters of geotechnical excavation after unloading.

Geotechnical type	Percentage of cumulative unloading (%)	Density (g/cm^3)	Modulus of elasticity (MPa)	Poisson's ratio	Cohesion (MPa)	Internal friction angle (degree)
Adamic earth	30	1.75	296.17	0.37	0.04697	11.71
Adamic earth	50	1.75	289.77	0.40	0.02308	10.32
Strongly weathered dolomite	30	1.9	296.17	0.35	0.06501	25.45
Strongly weathered dolomite	50	1.9	289.77	0.37	0.03194	22.44
Moderately weathered dolomite	30	2.5	493.61	0.28	0.08126	29.69
Moderately weathered dolomite	50	2.5	425.85	0.29	0.03993	26.18

The equivalent thickness of the plate, obtained from Equation (2), was approximately $h \approx 0.204$ m. The axial stiffness of the unit-width plate can be calculated as follows:

$$\mathrm{EA} = 30\ \mathrm{GPa} \times 0.204\ \mathrm{m}^2 = 6.12 \times 10^6\ \mathrm{kN}, \tag{3}$$

$$\mathrm{EI} = \frac{\mathrm{EA} \times h^2}{12} = \frac{6.12 \times 10^6 \times 0.204^2}{12} = 2.1224 \times 10^4 \mathrm{kN} \cdot \mathrm{m}^2. \tag{4}$$

The volumetric weight of the unit-width plate is given as follows:

$$25 \times 0.204 = 5.1\ \mathrm{kN/m}^3. \tag{5}$$

Based on Liu's [27] and Song et al.'s [28] studies, the physical and mechanical parameters of the gravity retaining wall were determined, as presented in Table 3.

Referring to the research findings of Li [29] regarding the degradation of rock and soil parameters due to unloading, the cumulative unloading percentage Δ was initially calculated based on the maximum principal stress at the representative point on the slope surface:

$$\Delta = \frac{P}{\sigma_0} \times 100\%, \tag{6}$$

where P represents the excavation unloading amount, which was the difference between the maximum principal stress at the representative point before excavation and after excavation; σ_0 represents the initial load applied prior to excavation.

Subsequently, the reduction percentage of elastic modulus (ψ_E), the increase percentage of Poisson's ratio (ψ_μ), the reduction percentage of cohesion (ψ_c), and the reduction percentage of internal friction angle (ψ_φ) were calculated using the following equations [30]:

$$\psi_E = 5.577\Delta^6 - 23.554\Delta^5 + 30.109\Delta^4 - 14.043\Delta^3 + 2.2156\Delta^2 + 0.0044\Delta + 0.0005, \tag{7}$$

$$\psi_\mu = 56.357\Delta^6 - 110.81\Delta^5 + 69.086\Delta^4 - 7.936\Delta^3 - 5.6006\Delta^2 + 1.625\Delta + 0.0007, \tag{8}$$

$$\psi_C = -78.306\Delta^6 + 239.45\Delta^5 - 267.73\Delta^4 + 128.5\Delta^3 - 22.586\Delta^2 + 1.3205\Delta - 0.0017, \tag{9}$$

$$\psi_\varphi = 24.478\Delta^6 - 57.537\Delta^5 + 47.312\Delta^4 - 16.872\Delta^3 + 2.4145\Delta^2 + 0.4355\Delta - 0.0019. \tag{10}$$

Building upon the initial elastic modulus (E_0), Poisson's ratio (μ_0), cohesion (c_0), and internal friction angle (φ_0), and applying Equations (7)–(10), the postunloading values of elastic modulus (E_u), Poisson's ratio (μ_u), cohesion (c_u), and internal friction angle (φ_u) were calculated as follows:

$$E_u = E_0(1 - \psi_E), \tag{11}$$

$$\mu_u = \mu_0(1 - \psi_\mu), \tag{12}$$

$$c_u = c_0(1 - \psi_c), \tag{13}$$

$$\varphi_u = \varphi_0(1 - \psi_\varphi). \tag{14}$$

Table 4 lists the geotechnical physical and mechanical parameters for cumulative unloading percentages of 30% and 50%. To monitor the displacement and stress of the slope during excavation, Model I had 15 monitoring points arranged on the slope surface (Figure 4).

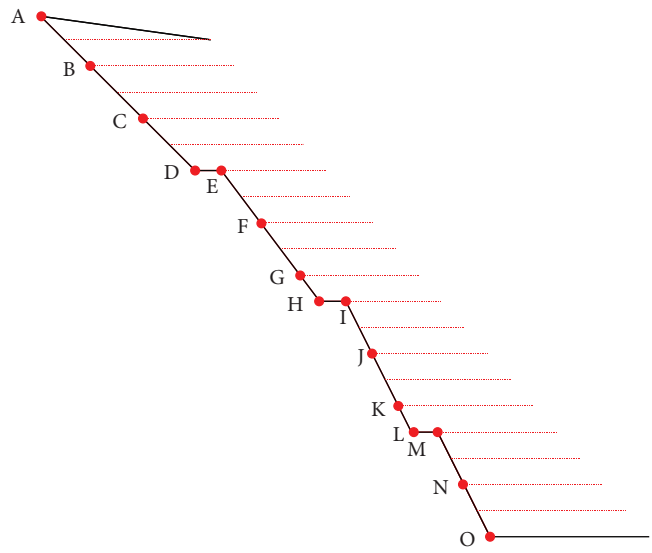

Figure 4: Location of monitoring points for displacements and stresses during slope excavation.

3.2. Scheme of the Calculation Model. This study presents three computational approaches designed to assess the impact of multistage artificial excavation on the stability of bedding cataclastic rock mass high slope containing multimuddy interlayers, taking into account support mechanisms and the deterioration of geotechnical parameters.

Scheme 1: The slope with muddy interlayers was excavated without support and without considering geotechnical parameter deterioration. The scheme acknowledged the effects of the muddy interlayers; however, it neither implemented support following the excavation of the slope nor considered the degradation of geotechnical parameters due to unloading caused by the excavation.

Scheme 2: After the excavation of the slope with muddy interlayers, it was supported but without considering geotechnical parameter deterioration. The scheme acknowledged the effects of the muddy interlayers, providing immediate reinforcement postexcavation of each slope level, yet it failed to take into account the deterioration of geotechnical parameters arising from unloading during excavation.

Scheme 3: The slope with muddy interlayers was excavated without support but with consideration to geotechnical parameter deterioration. The scheme acknowledged the effects of the muddy interlayers, yet did not implement any support after the excavation of the slope, though it did consider the impact of excavation-induced unloading on the deterioration of geotechnical parameters.

4. Results and Discussion

4.1. Stability of Slopes with Muddy Interlayers, Unsupported and Unadjusted for Geotechnical Parameter Deterioration (Scheme 1). First, it was noted that when the cataclastic rock mass slope containing muddy interlayers was excavated without support, it became unstable by the 25th step of excavation. This destabilization occurred within the elevation range of 1,835–1,837 m, which was lower than the actual recorded elevation where instability was observed.

Figure 5 displays the maximum shear stress diagrams following certain excavation steps. As the slope was excavated step by step and layer by layer, a growing concentration of shear stress became apparent. After the excavation halted at the 25th step, a pronounced concentration of shear stress was evident in the first and second levels of the slope, as well as in the underlying muddy interlayers, as highlighted in Figure 5(d). The maximum shear strain progressively increased with the continuation of the excavation. Once the excavation was completed, the maximum shear strain was observed in the exposed muddy interlayer closest to the slope base, as illustrated in Figure 6.

The horizontal displacement diagram for the first computational scenario (Figure 7) indicates: (1) Before the muddy interlayer was excavated and exposed, the horizontal displacement of the slope was primarily caused by the relative sliding of the underlying rock layer. After the interlayer was exposed on the slope surface, the slope's horizontal displacement was mainly due to the relative sliding along the interlayer. (2) The horizontal displacement between the rock layer containing muddy interlayers and the underlying cataclastic rock layer was discontinuous. Similarly, the horizontal displacement between the muddy interlayer and the cataclastic rock mass was also discontinuous, exhibiting multiple layers of relative slippage.

A careful examination of Figure 8 reveals:

(1) Before the muddy interlayers were excavated and exposed (steps 1–10), using point C as a boundary, the horizontal displacements of the monitoring points above were negative. The displacement increased progressively, with the maximum value occurring at the top of the slope at point A. In contrast, the monitoring points below point C exhibited positive horizontal displacements, increasing gradually, with the peak value at point F. This indicated that the upper part of the slope tilted backward, while the lower part slid toward

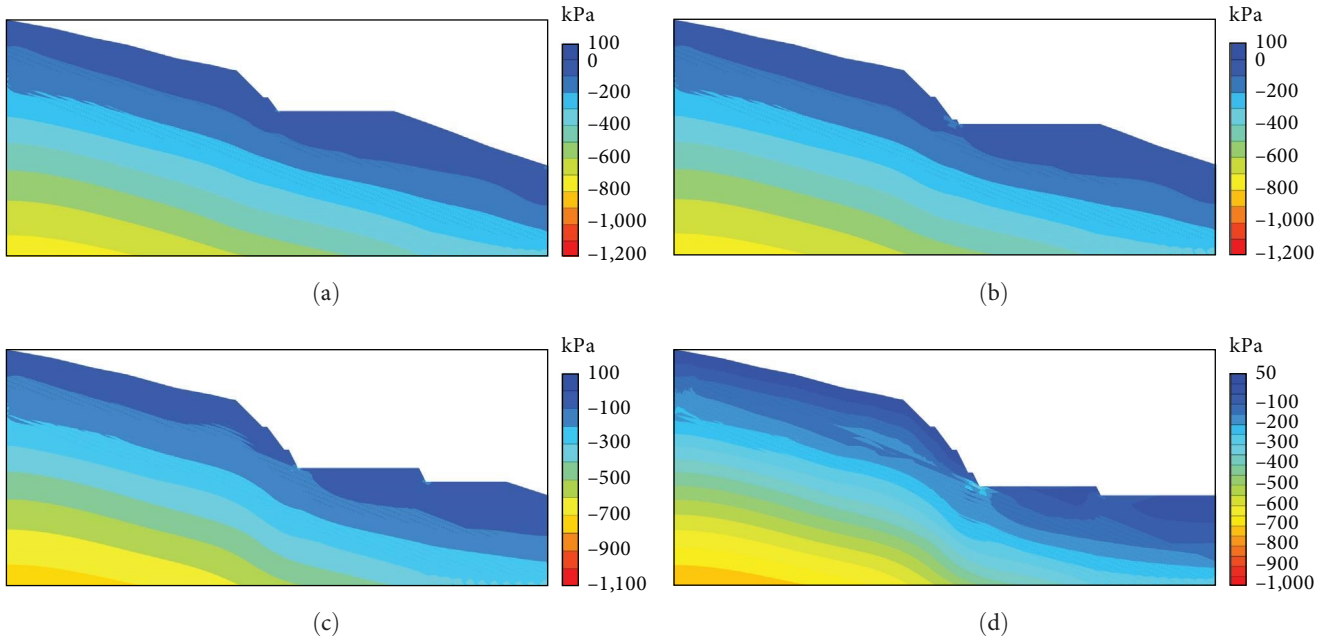

Figure 5: Maximum shear stress plot for Model I 1st calculation scheme. (a) Step 9 after excavation. (b) Step 12 after excavation. (c) Step 18 after excavation. (d) Step 25 after excavation.

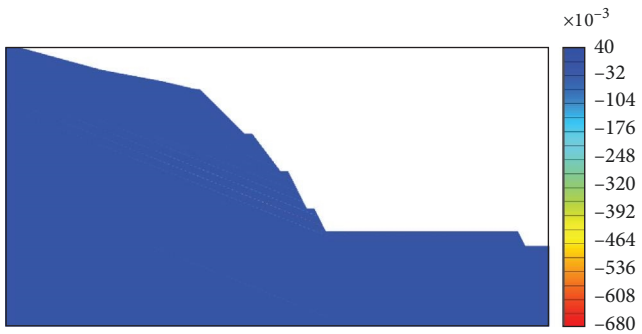

Figure 6: Maximum shear strain plot for Model I 1st calculation scheme (magnification 15x).

the exposed face. (2) After the 11th step of excavation, the horizontal displacement at the base point H had not increased significantly. However, there was a clear slide of the slope surface points toward the exposed face, especially at point G. With subsequent layer-by-layer excavation, the more muddy interlayers that were exposed on the slope surface, the greater the relative sliding of the slope along these muddy interlayers. (3) The excavation on the outer side of the first and second levels of the slope (steps 16–21) caused all monitoring points to move toward the exposed face. The displacement of the slope surface points was greater than that of the unexposed monitoring points. (4) From steps 21–24, more muddy interlayers were exposed on the slope surface, leading to even greater displacements of the slope surface points toward the exposed face, especially at points G, H, I, and J, which were closer to the slope base. The horizontal displacement at the base of the slope was not the greatest because the muddy interlayers did not pass through the base of the slope, and the downward sliding of the slope along the muddy interlayers was hindered by the large platform in front of the slope base. The horizontal displacement at the slope top was not as significant as that at the front edge of the slope. An increase in the displacement at the front edge to a certain value could lead to tensile cracking at the rear edge of the slope. (5) After the 25th step of excavation, the front and rear edges of the slope experienced the greatest increases in horizontal displacement. The differences in horizontal displacement among the slope surface monitoring points were not significant, indicating that the slope had sheared along the base and the rear edge had experienced tensile cracking. The slope had become unstable.

As shown in Figure 9, before the muddy interlayers were excavated and exposed (steps 1–10), the maximum horizontal displacement in the positive X-direction of the slope increased slowly to 4.694 mm. During the excavation of the second level slope, the displacement increased uniformly to 26.18 mm. The excavation of the outer side of the slope did not have a significant impact on the horizontal displacement. During the excavation process of the first level slope, the displacement rapidly increased to 109 mm, leading to failure and instability. The analysis above suggests that the excavation processes of the first and second level slopes significantly affected the maximum horizontal displacement in the positive X-direction of the slope.

As observed from the slope mesh deformation diagram (Figure 10), before the muddy interlayers were excavated and exposed, the slope body slid along the underlying muddy interlayers. Due to the restraining effect of the large platform in front of the slope base, the rock layer at the slope base underwent a bending and bulging deformation, while the slope top tilted backward in contrast. With progressive layer-by-layer excavation, the depth of the muddy interlayers

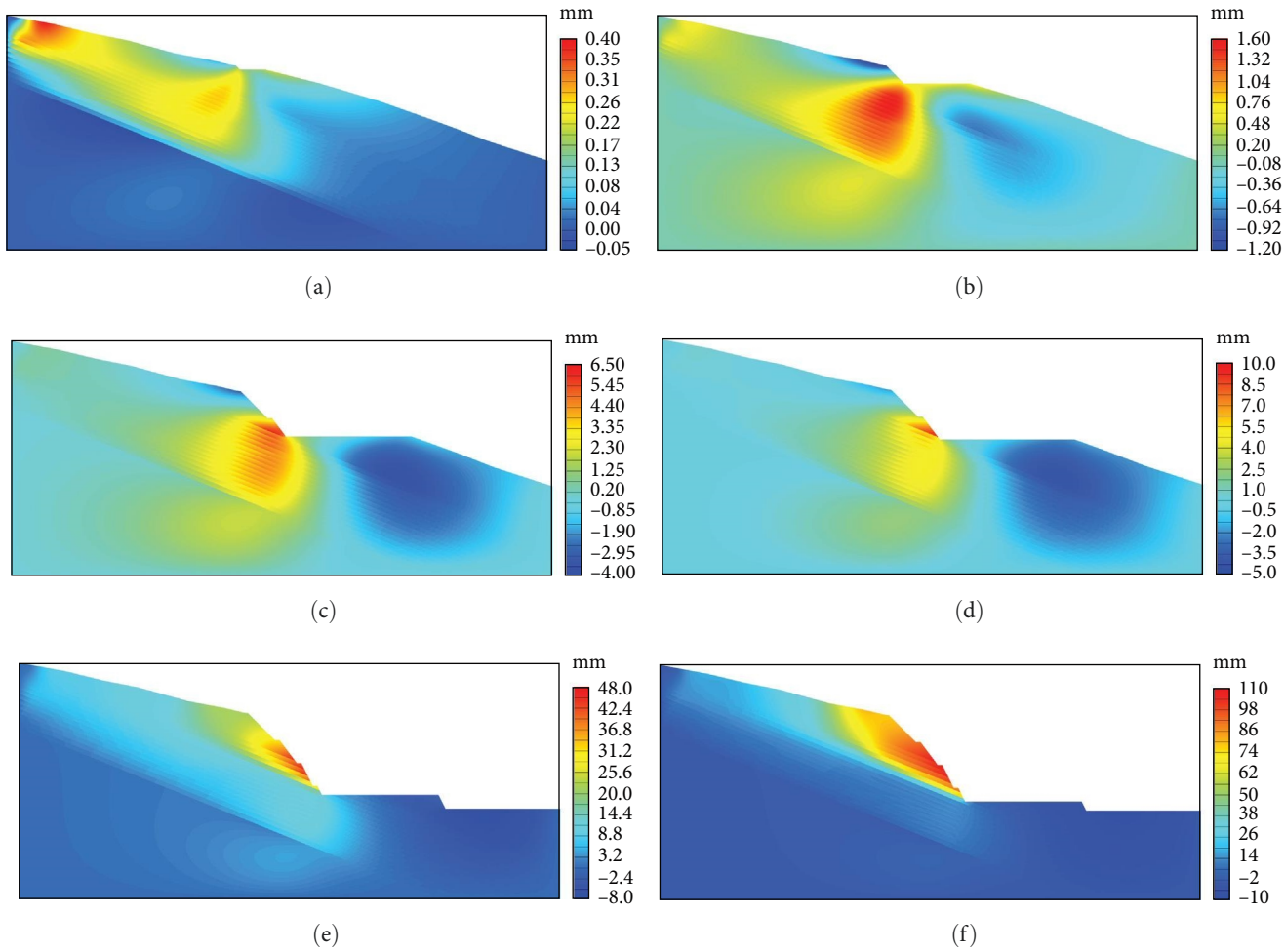

Figure 7: Horizontal displacement plot for Model I 1st calculation scheme. (a) Step 1 after excavation. (b) Step 4 after excavation. (c) Step 10 after excavation. (d) Step 11 after excavation. (e) Step 24 after excavation. (f) Step 25 after excavation.

decreased. The bending and bulging deformation of the rock layer at the slope base became more pronounced, and the backward tilting of the slope top also became more noticeable (Figures 10(a) and 10(b)). After the muddy interlayers were exposed on the slope surface, the slope body primarily exhibited relative shear sliding along the muddy interlayer. The more the muddy interlayers were exposed, the larger the relative sliding amount became. The location with the maximum sliding amount was at the front edge of the slope (Figure 10(c)–10(e)). As a result, this led to tensile rupture and damage at the rear edge of the slope. After the 25th excavation step, the slope became unstable. The sliding shear outlet was located at the lowest exposed muddy interlayer on the slope face (Figure 10(f)).

As observed from Figure 11, in scheme 1, the safety factor of the slope decreased to 1.328 after the 10th excavation step. After the 11th excavation step, when the muddy interlayer started to become visible on the slope face, the safety factor decreased to 1.225, which was slightly lower than 1.35. During the excavation of the second level slope, the safety factor gradually decreased to 1.044, indicating that the slope was in a critically unstable state. Any minor disturbance could potentially result in slope failure. The impact of excavation on the outer side of the slope on the safety factor was negligible. After the excavation steps from the 22nd to the 24th on the first level slope, the safety factor dropped to 0.93. The slope became unstable after the 25th excavation step.

Observations from Figures 9 and 11 revealed that the maximum horizontal displacement in the X-direction of the bedding cataclastic rock mass slope with multimuddy interlayers was not significant during the third and fourth stages of excavation. However, this displacement rapidly increased during the first and second stages. While the safety factor improved during the excavation of the fourth stage, it decreased rapidly in the third stage, dropping slightly below 1.35. The safety factor gradually decreased during the second stage and decreased rapidly during the first stage, leading to instability in the first stage slope before the completion of the planned excavation. The horizontal displacement at the forefront of the slope, toward the overhanging face, was greater than that at the rear, as shown in Figure 11. This analysis suggested that for the bedding cataclastic rock mass slope with multimuddy interlayers, the third and fourth stage slopes could remain unsupported, with the focus having

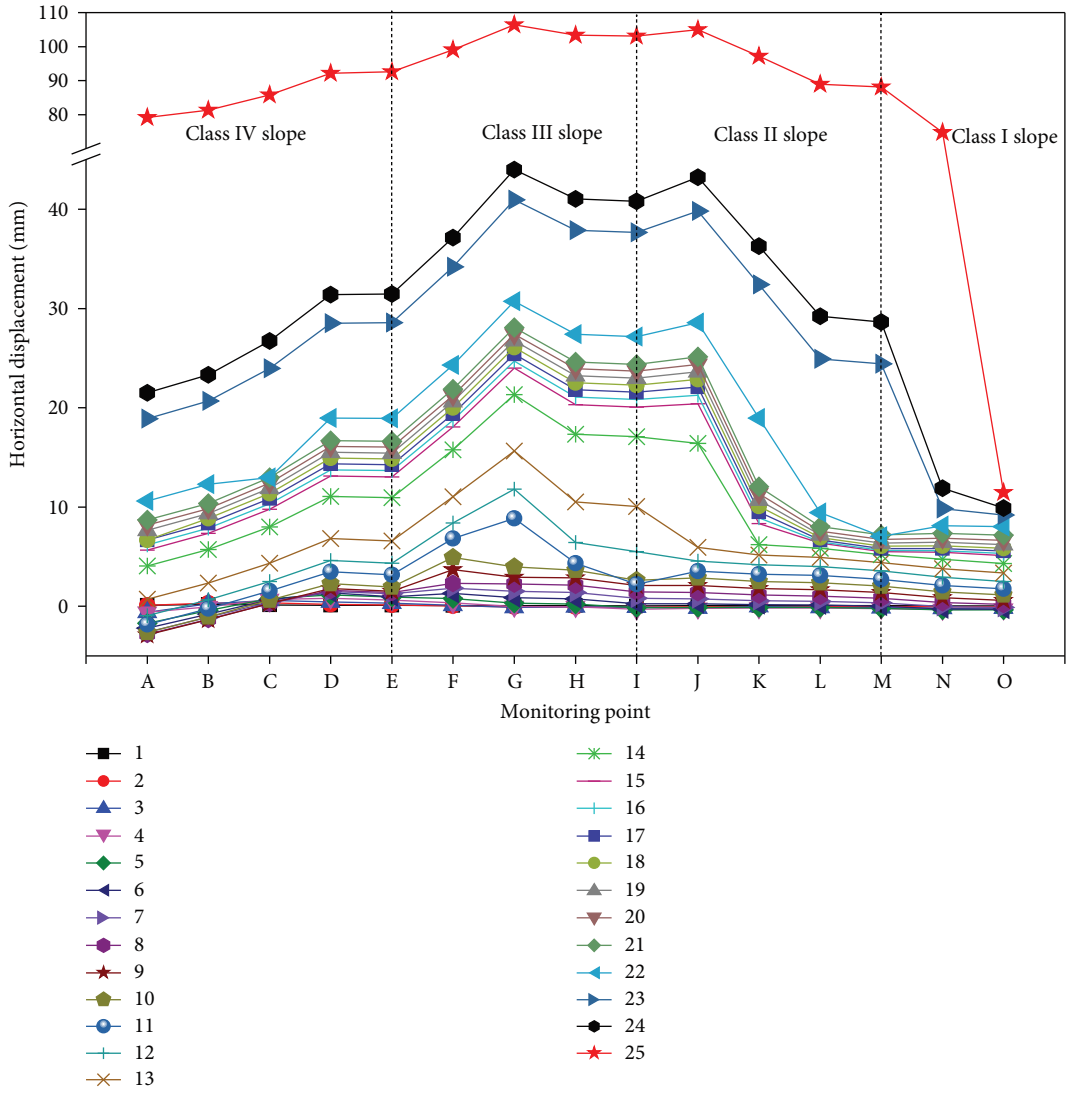

Figure 8: Relationship between horizontal displacement and excavation step for 15 monitoring points of Model I 1st calculation scheme.

shifted to supporting the first and second stages. Reinforced support for the first stage slope was found to be particularly critical.

Combining the above analysis, for the bedding cataclastic rock mass slope containing multimuddy interlayers, the slope became unstable before completing the planned excavation (without support). As the slope was excavated layer by layer, the maximum shear strain and horizontal displacement of the slope gradually increased. There was an increasing concentration of stress, a gradual decrease in the safety factor, and a trend of transitioning from a compressed stress state to a tensile stress state in the slope stress environment. The displacement in the positive X-direction of the slope was greater than in the negative X-direction. Under the excavation disturbance, the bedding cataclastic rock mass slope containing multimuddy interlayers underwent deformation, including foot bending and uplift, toppling backward at the slope top, and multilayer relative shear sliding. The failure instability mode involved bending uplift-multilayer shear sliding- and rear-edge tensile cracking.

4.2. Stability of the Slope with Muddy Interlayers, Supported but Without Considering Geotechnical Parameter Deterioration (Scheme 2). First, it should be noted that after the excavation and support of bedding cataclastic rock mass high slope containing multimuddy interlayers, this study did not consider the degradation of the geotechnical parameters. The slope could be completed and maintained stably according to the design of excavation and support. However, the safety factor of the slope had decreased to 1.121, indicating that the safety reserve was insufficient. In this simulation, the support was implemented after the completion of excavation for each level of the slope.

From the maximum principal stress diagram of the slope under the second calculation scheme (Figure 12), it was observed that: (1) As the slope was excavated layer by layer, the tensile stress gradually increased. After the 25th step of excavation, the tensile stress had reached 22.78 kPa. After the 26th step of excavation, the tensile stress suddenly increased to 156.9 kPa, appearing at the contact point between the top of the gravity retaining wall and the soil–rock mass. This

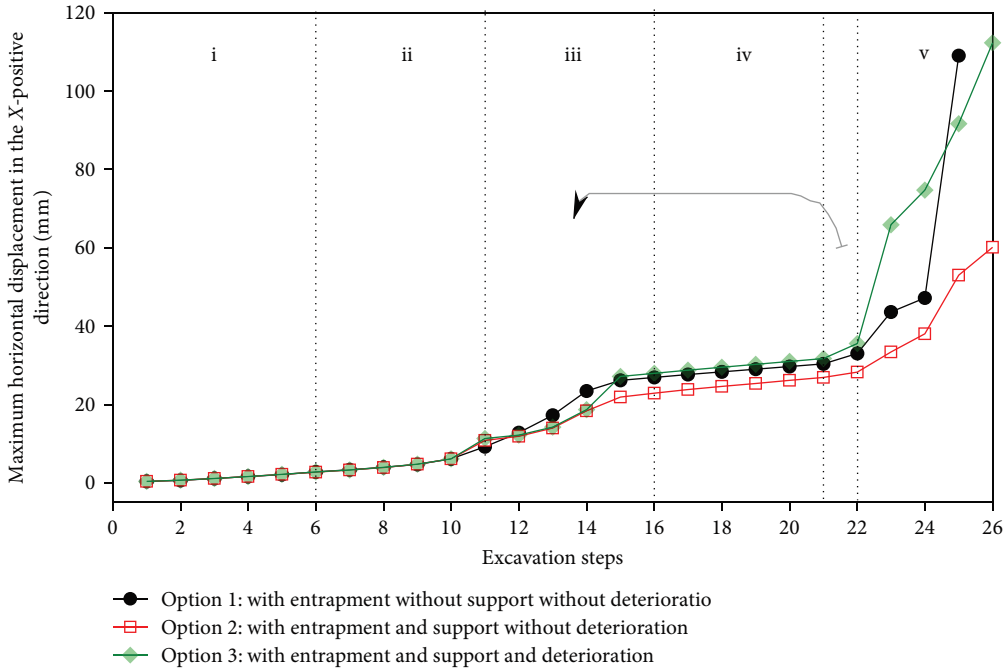

Figure 9: Relationship between the maximum horizontal displacement in the X-positive direction and the excavation step for the three calculation schemes of Model I ((i) class 4 slope excavation, (ii) class 3 slope excavation, (iii) class 2 slope excavation, (iv) excavation on the outside of a grade 1 or 2 slope, and (v) class 1 slope excavation).

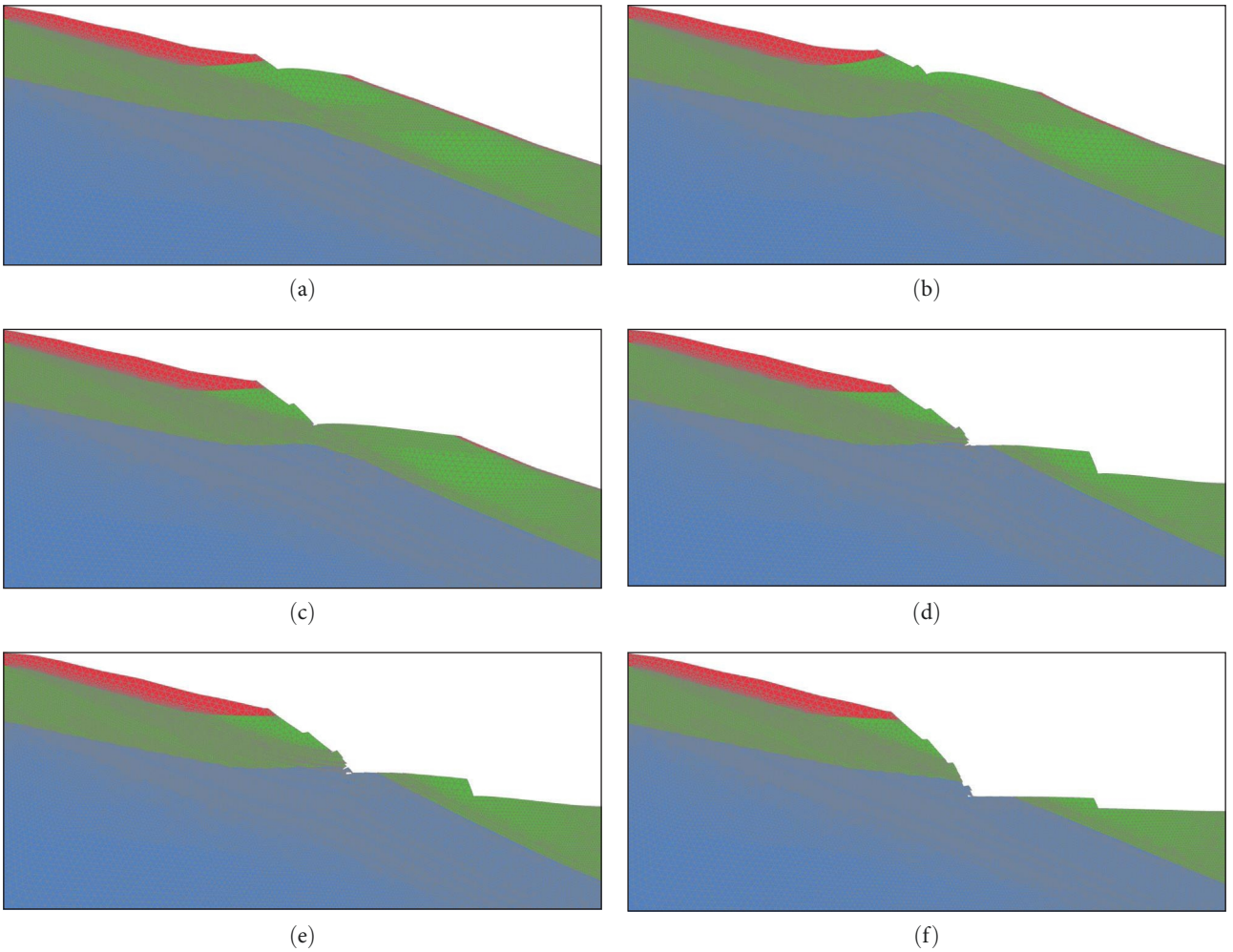

Figure 10: Slope grid deformation diagram for Model I 1st calculation scheme. (a) Step 4 after excavation. (b) Step 8 after excavation. (c) Step 11 after excavation. (d) Step 23 after excavation. (e) Step 24 after excavation. (f) Step 25 after excavation.

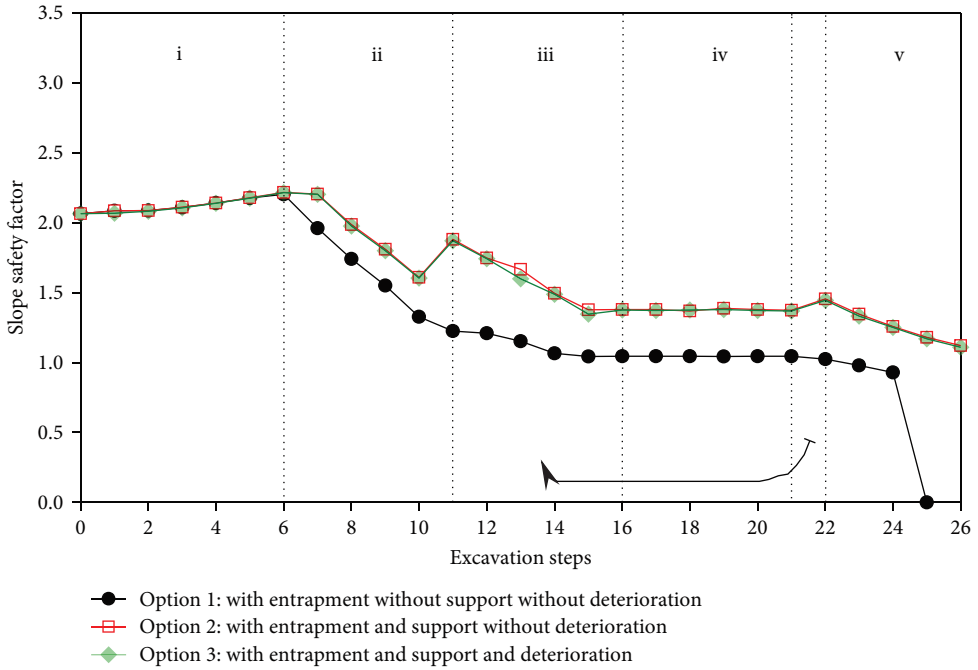

Figure 11: Relationship between slope safety factor and excavation steps for three calculation schemes of Model I ((i) class 4 slope excavation, (ii) class 3 slope excavation, (iii) class 2 slope excavation, (iv) excavation on the outside of a grade 1 or 2 slope, and (v) class 1 slope excavation).

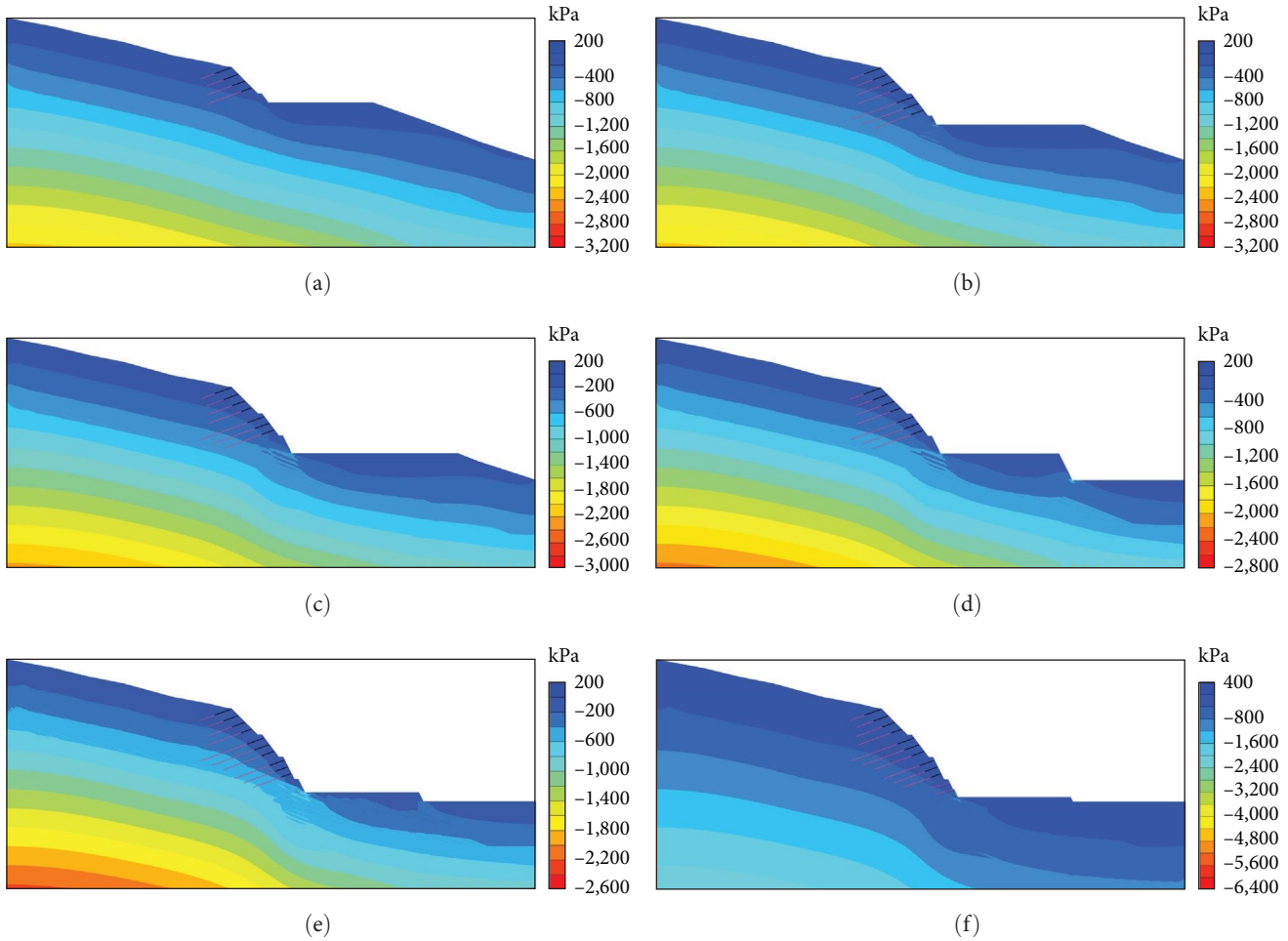

Figure 12: Maximum principal stress plot for Model I 2nd calculation scheme. (a) Step 8 after excavation. (b) Step 13 after excavation. (c) Step 15 after excavation. (d) Step 21 after excavation. (e) Step 25 after excavation. (f) Step 26 after excavation.

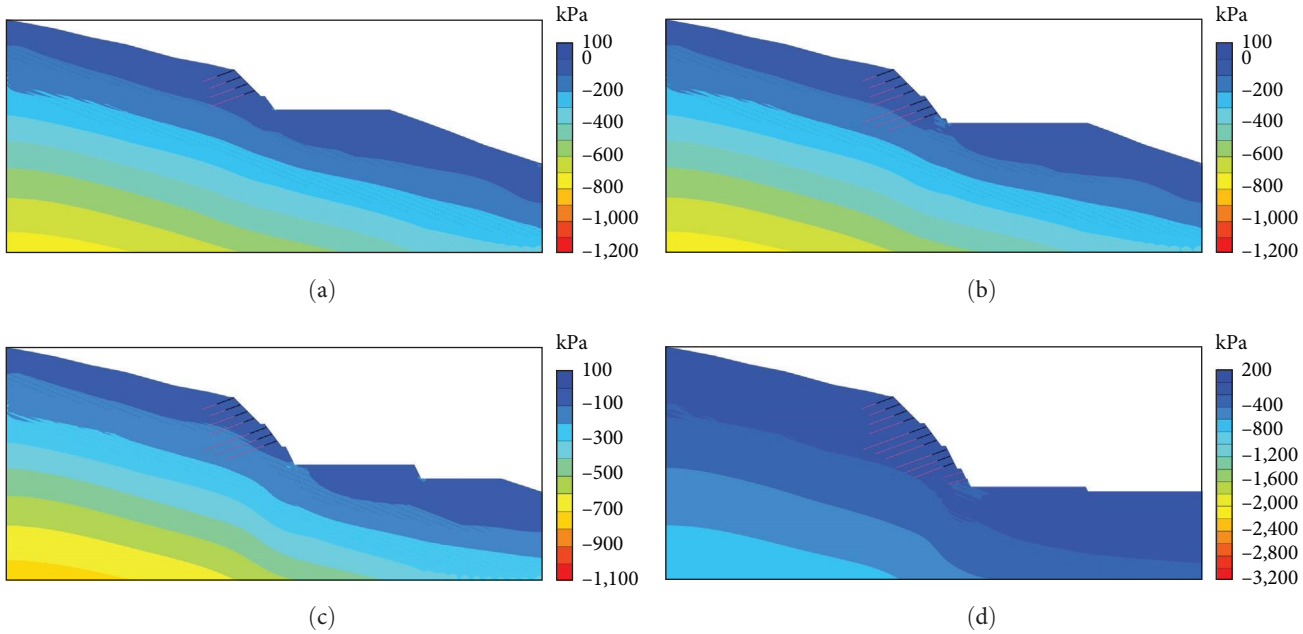

Figure 13: Maximum shear stress plot for Model I 2nd calculation scheme. (a) Step 9 after excavation. (b) Step 12 after excavation. (c) Step 18 after excavation. (d) Step 26 after excavation.

indicated that the gravity retaining wall and the soil–rock mass behind the wall had already separated. (2) After the 26th step of excavation, the compressive stress also abruptly increased, appearing at the back of the gravity retaining wall, with a value of −6.296 MPa. This value was significantly greater than the design compressive strength of the mortar masonry stones [31], indicating that the retaining wall might have been compromised due to compression.

The shear stress plots and their evolution for the second calculation scheme (Figure 13) were similar to those for the first calculation scheme (Figure 5). The most notable difference was that after the 26th step of excavation and support, the maximum shear stress at the contact area between the mortar masonry stone retaining wall and the muddy interlayers abruptly increased, with a value of −3.006 MPa. This increase was attributed to the relative sliding of the slope along the interlayers and the resultant interaction between the slope and the support structure.

As shown in Figure 9: (1) Similar to scheme 1, in scheme 2, the horizontal displacement in the positive X-direction of the slope primarily occurred during the excavation of the first and second levels of the slope, especially during the excavation of the first level. This suggests that the horizontal displacement in the positive X-direction of the slope was mainly affected by the excavation of the first and second levels, while the effects of other excavation steps were not significant. (2) After the 25th step of excavation in scheme 1, the slope had become entirely unstable. In contrast, scheme 2 had not reached full instability, indicating that the supporting measures had been able to reduce the horizontal displacement of the slope.

As shown in Figure 14: (1) After the excavation and support of the fourth-level slope, the horizontal displacement of the toe point D decreased, while the slope surface moved backward, with the maximum displacement observed at the top point A. (2) The excavation of the third-level slope led to the sliding of this slope section toward the exposed face. However, the third-level platform barely moved in the horizontal direction. After the support was implemented, both the third-level slope and the platform moved backward, which was beneficial for the stability of the slope. (3) The excavation of the second-level slope and the external side of the slope caused the entire slope to move toward the exposed face. The largest displacement was observed at monitoring point J. After the support was implemented for this level of the slope, the entire slope moved toward the back of the slope. (4) The excavation of the first-level slope led to a significant movement of the slope toward the exposed face. The displacement increased gradually from the upper to the lower part of the slope, with the maximum value located at point N near the toe of the slope. This was due to the primary movement of the slope along the exposed muddy interlayers on the slope face. (5) After the support of the first-level slope, the slope still moved significantly toward the exposed face as a whole, indicating that the support of the first-level slope could not improve the stability of the slope.

In terms of the grid deformation of the slope, the supporting structure in scheme 2 deformed (Figure 15): (1) The grid beams of the third-level slope exhibited bending deformation, while the grid beams of the second-level slope underwent shear displacement. (2) The anchor cables and rock bolts experienced shear displacement and elongation deformations at the positions where they passed through the muddy interlayers; (3) the closer to the toe of the slope, the greater the deformation of the supporting structure.

Under normal conditions, with regard to the distribution of the plastic zone: In scheme 1, the maximum plastic strain was primarily distributed in the lowest exposed muddy

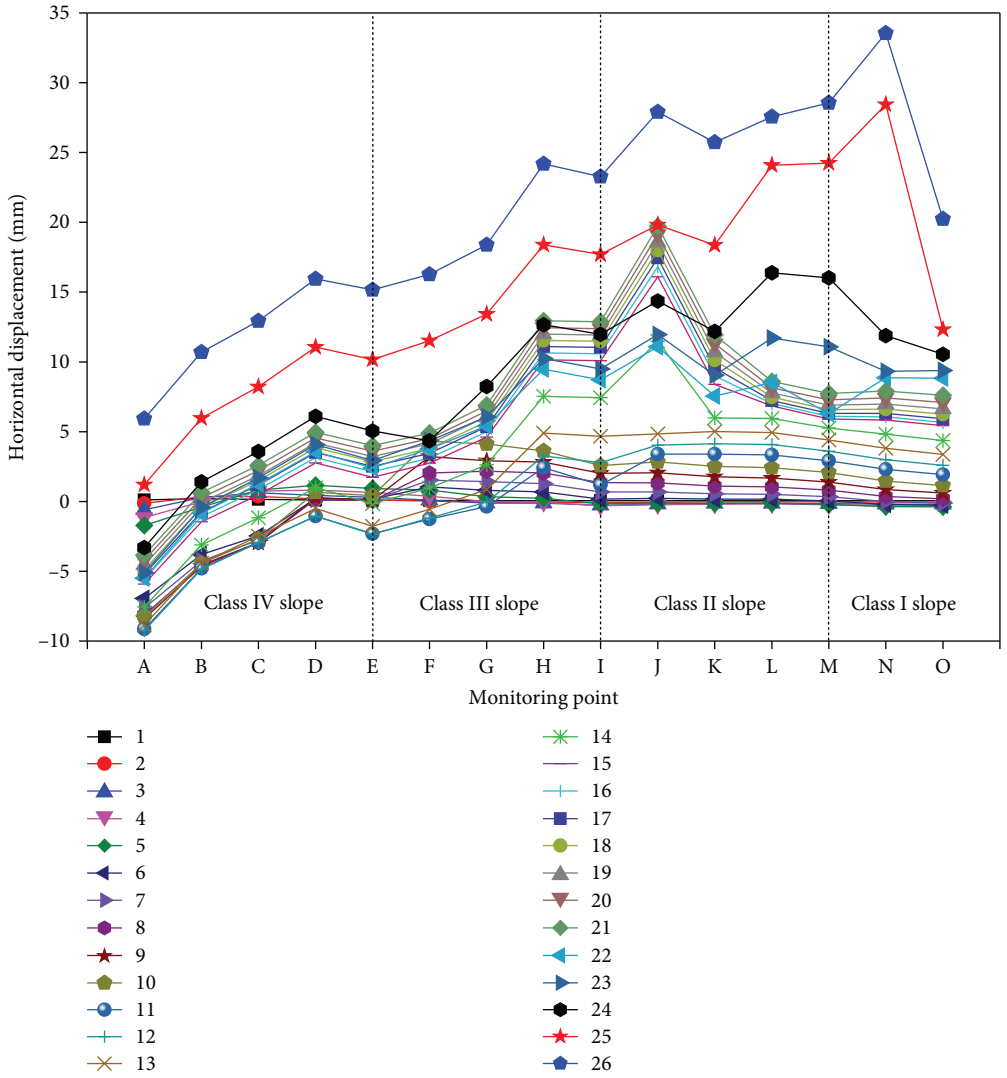

Figure 14: Relationship between horizontal displacement and excavation step for 15 monitoring points of Model I 2nd calculation scheme.

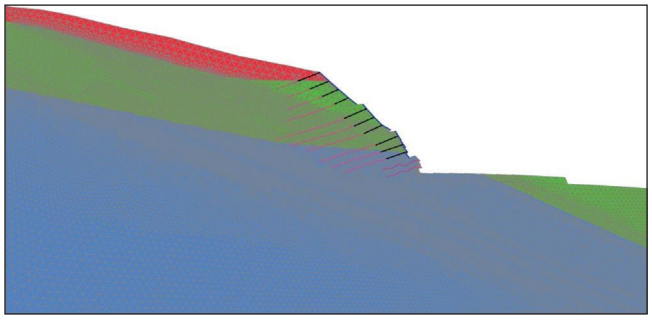

Figure 15: Slope grid deformation diagram for Model I 2nd calculation scheme.

interlayer on the slope face (Figure 16(a)). In scheme 2, the maximum plastic strain mainly occurred in the first muddy interlayer beneath the toe of the slope (Figure 16(b)). The plastic strain in scheme 2 was smaller than that in scheme 1, indicating that implementing support after excavation was beneficial for the stability of the slope. The above analysis indicated that for the bedding cataclastic rock mass slope containing multimuddy interlayers, regardless of whether there was support after excavation, the potential instability mode of the slope was sliding along the muddy interlayers. However, with support in place, the potentially sliding muddy interlayers were concealed below the slope surface, which was favorable for slope stability. This indicates that the supporting measures indeed improved the stability of the slope.

Integrating the research outcomes of solutions 1 and 2, it was concluded that the support measures in Model I were characterized by inadequate support arrangement and insufficient support strength. The third and fourth stage slopes could remain unsupported, and emphasis was placed on reinforcing the support for the first and second stage slopes, particularly the first stage slope, rather than weakening the support for the first stage slope. Therefore, we recommended that, for the bedding cataclastic rock mass slope containing multimuddy interlayers, the slope above the exposure of

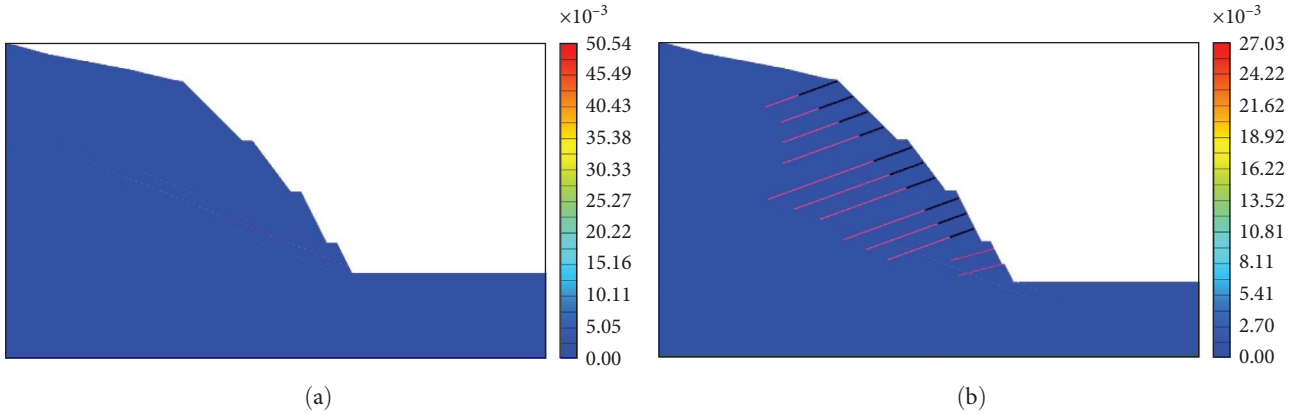

Figure 16: Plasticity zone distribution map. (a) Distribution of plastic zones in the normal state of scheme 2. (b) Distribution of plastic zones in the normal state of scheme 3.

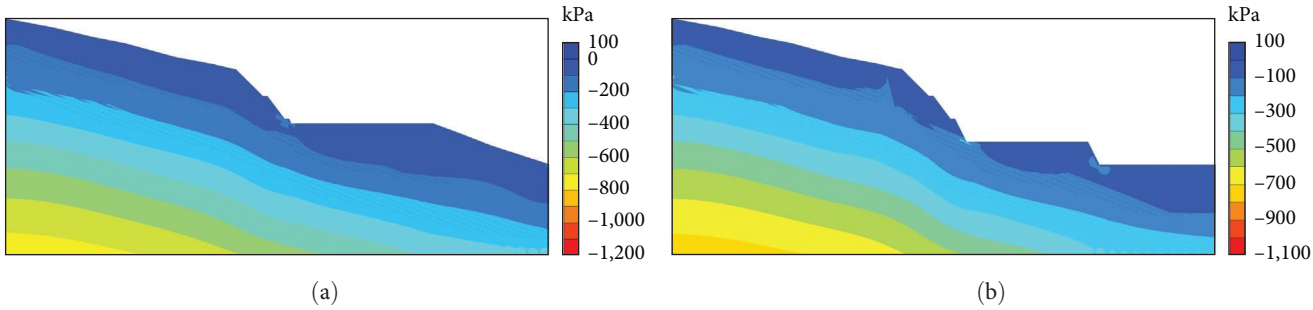

Figure 17: Maximum shear stress diagram for calculation scheme 3. (a) Step 12 after excavation. (b) Step 22 after excavation.

muddy interlayers could remain unsupported, while the slope below the exposure of muddy interlayers was prioritized for support. The support intensity gradually increased toward the foot of the slope.

4.3. Stability of Slopes with Muddy Interlayers, Unsupported but Considering Parameter Deterioration (Scheme 3). In scheme 1, the slope became unstable during the excavation at elevations ranging from 1,835 to 1,837 m, while in scheme 3, the slope had already become unstable by the 22nd step of excavation, specifically within the elevation range from 1,841 to 1,843 m. This is consistent with the actual situation of slope instability. This indicated that when using numerical simulation methods to study the impact of excavation disturbances on the stability of bedding cataclastic rock slopes embedded with multiple muddy interlayers, it was necessary to consider the degradation of geotechnical parameters to obtain simulation results closely aligned with actual conditions. The degradation of geotechnical parameters in the excavation relaxation zone reduced the stability of the slope.

In terms of the maximum shear stress distribution, the following observations were made after the 12th step of excavation: Shear stress concentration began to appear at the toe of the slope and gradually evolved toward the slope face and the underlying mud interlayer as the excavation proceeded step by step (Figure 17(a)). After the 22nd step of excavation, shear stress concentration was observed at the boundary between the relaxed and nonrelaxed zones of the slope.

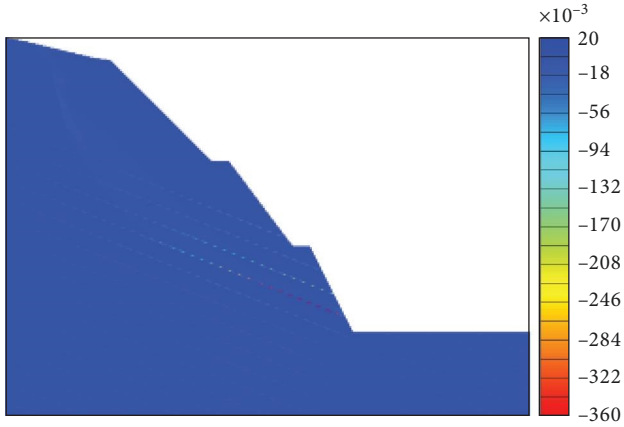

Figure 18: Maximum shear strain after completion of excavation for scheme 3 of Model I (magnification 20x).

This was distinct from scheme 1 and could potentially lead to rear-edge failure of the slope (Figure 17(b)).

For scheme 3, the maximum shear strain of the slope progressively increased as the excavation continued. After the cessation of excavation, the maximum shear strain was located in the revealed muddy interlayers nearest to the toe of the slope (Figure 18). This was smaller than that in scheme 1, amounting to 55% of the latter. A significant difference, compared to scheme 1, was the appearance of an arc-shaped

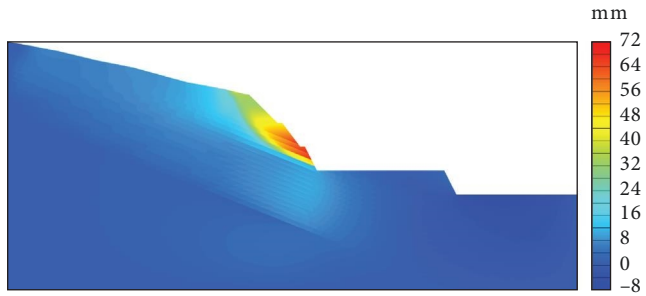

Figure 19: Horizontal displacement after excavation in step 22 of Model I scheme 3.

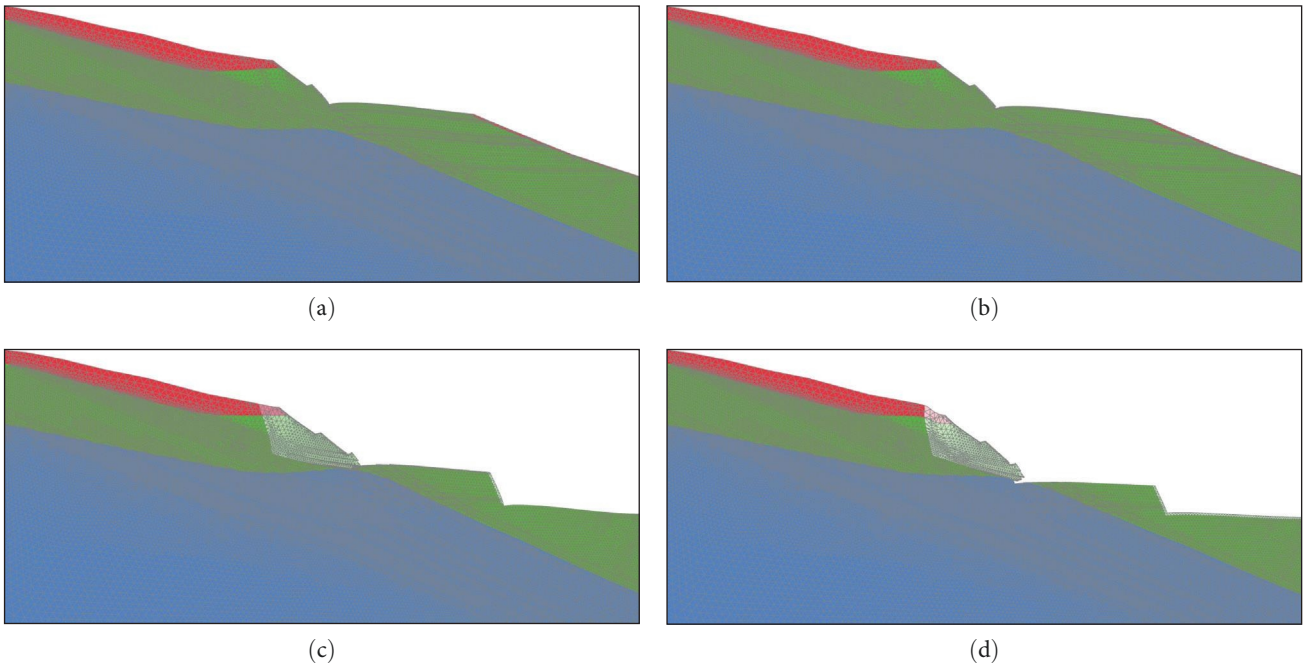

Figure 20: Partial slope grid deformation map for the 3rd calculation scheme. (a) Step 10 after excavation. (b) Step 11 after excavation. (c) Step 21 after excavation. (d) Step 22 after excavation.

light blue band within the deep blue background at the top rear edge of the slope, indicating the presence of an arc-shaped shear band in the slope (Figure 18).

In terms of the horizontal displacement field: (1) The evolution pattern of the horizontal displacement field in scheme 3 was similar to that in scheme 1. (2) The maximum horizontal displacement in the X-direction gradually increased with stepwise excavation. (3) After the cessation of excavation, the maximum horizontal displacement in the X-direction for scheme 3 was 63% of that in scheme 1, owing to the reduced height of the slope in scheme 3 at the time of failure. (4) After the 22nd step of excavation in scheme 3, the horizontal displacement was mainly concentrated in the second and third levels of the slope (Figure 19), while in scheme 1, high horizontal displacement was observed throughout the entire slope (Figure 7(f))

Regarding the maximum horizontal displacement in the X-direction (Figure 9): Prior to the 14th step of excavation, there was a little difference between schemes 3 and 1. From the 15th to the 21st step, the displacement in scheme 3 was approximately 4.8 mm greater than in scheme 1. After the 22nd step of excavation, the displacement in scheme 3 suddenly increased, being 35.9 mm greater than in scheme 1.

The mesh deformation of the slope in scheme 3 was similar to that in scheme 1. Prior to the exposure of the muddy interlayers, the primary deformation observed was the bending and bulging of the rock layer, with the top of the slope tilting backward (Figures 20(a) and 20(b)). After the exposure of the muddy interlayers, the predominant deformation mode was shearing and sliding of the slope along the muddy interlayers. Notably, the maximum shear displacement was not located at the toe of the slope but rather in the second muddy interlayers near the toe (Figures 20(c) and 20(d)).

Prior to the 14th excavation step, the safety factors of schemes 3 and 1 were nearly equal. Subsequent to this, the safety factor of scheme 3 became slightly lower than that of scheme 1. After the 22nd excavation step, the safety factor of scheme 3 suddenly dropped to 0.6, which was 0.4 lower than that of scheme 1 (Figure 11).

Under normal conditions, the distribution of plastic zones in scheme 3 differed from that in scheme 1. In scheme 1,

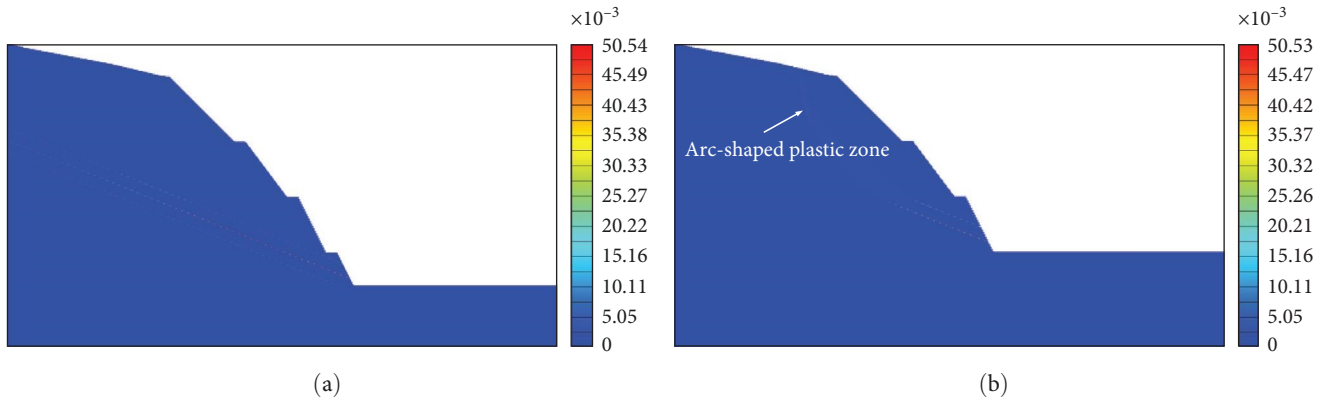

Figure 21: Plasticity zone distribution map. (a) Distribution of plastic zones in the normal state of scheme 1. (b) Distribution of plastic zones in the normal state of scheme 3.

plastic deformation primarily occurred in the muddy interlayers near the toe of the slope. In contrast, while scheme 3 also exhibited plastic deformation in the muddy interlayers near the toe of the slope, the distribution length was less than that in scheme 1. Notably, scheme 3 showed the emergence of a circular arc-shaped plastic zone at the rear edge of the slope (Figure 21). Based on a comprehensive analysis of the maximum shear stress diagrams, maximum shear strain diagrams, horizontal displacement plots, and plastic zone distribution maps, it was inferred that the slope failure under scheme 3 was initiated by local instability, leading to a landslide. This process prominently involved the transitional zone between the second and third slope levels. The key sequence of events was identified as follows: Initially, the sliding started from the second-tier platform along the muddy interlayers. This action subsequently caused the upper relaxed fractured rock mass of the slope to lose its support, and thereafter, this unsupported rock mass sheared along a circular sliding surface. For scheme 1, the entire slope slid along the muddy interlayers, with tension fractures forming at the rear edge of the slope. The simulation results under scheme 3 were found to align more closely with the actual landslide conditions of the high slope at the Yuxi Waste Incineration Power Plant.

Based on the comprehensive analysis, for the bedding cataclastic rock mass slope containing muddy interlayers left unsupported after excavation, compared to the condition without considering the degradation of rock mass parameters in the excavation loosening zone, the stability of the slope was worse when accounting for the deteriorated rock mass parameters. It was more prone to instability, with smaller horizontal displacement upon failure. The instability pattern involved initial sliding along the muddy interlayers in the lower part of the slope, followed by loss of support in the upper part leading to shear sliding failure along an arc-shaped sliding surface.

5. Conclusions

This study explored the effects of artificial multistage excavation on the stability of bedding cataclastic rock mass high slopes with multimuddy interlayers. Drawing on numerical simulation results, the paper presents its principal conclusions as follows:

(1) The presence of multimuddy interlayers was a significant factor contributing to the instability of the excavated slope. Consequently, the relationship between excavation and muddy interlayers is a focal point of concern in slope engineering, both in field surveys and construction. Minimizing the exposure of muddy interlayers during excavation is essential to prevent potential sliding.

(2) The horizontal displacement of the slope was primarily induced by the excavation of the first and second levels. Support measures significantly reduced this horizontal displacement. Therefore, for bedding cataclastic rock mass high slope containing multimuddy interlayers, slopes above the exposed muddy interlayers may not require reinforcement. In contrast, slopes below these interlayers should be prioritized for support, with increasing reinforcement strength toward the slope base.

(3) Local destabilization leading to landslides aligns more closely with the actual conditions of this slope. Specifically, the second-level platform initially slid along the muddy interlayers, resulting in the relaxation and fracturing of the rock mass above, which then sheared along a circular sliding surface. To accurately evaluate the stability of the slope, the evolution of the sliding surface during the excavation process should be given significant attention.

(4) In simulations considering the degradation of geotechnical parameters, the modeled landslide instability more closely aligned with the actual instability situation. Therefore, when using numerical simulations to study the impact of excavation on the stability of bedding cataclastic rock mass high slope containing multimuddy interlayers, it is imperative to consider the degradation of geotechnical parameters comprehensively to obtain simulations that closely mirror real-world conditions.

Data Availability

The data used to support the findings of this study are available from the corresponding author upon request.

Conflicts of Interest

The authors declare that they have no conflicts of interest.

Acknowledgments

This research was funded by the National Nature Science Foundation of China, grant number 41807258.

References

[1] B. Li, Y. Gao, Y. Yin et al., "Rainstorm-induced large-scale landslides in Northeastern Chongqing, China, August 31 to September 2, 2014," *Bulletin of Engineering Geology and the Environment*, vol. 81, no. 7, Article ID 271, 2022.

[2] S. R. Xiao, D. F. Liu, and Z. Y. Hu, "Study of high speed slide mechanism of Qianjiangping landslide in three gorges reservoir area," *Rock and Soil Mechanics*, vol. 31, no. 11, pp. 3531–3536, 2010.

[3] S. D. Li, X. Li, N. X. Zhang, and Y. H. Liu, "Water-rock interaction of clay gouged intercalation sludging process of baota landslides in Three Gorges reservoir area," *Rock and Soil Mechanics*, vol. 27, no. 10, pp. 1841–1846, 2006.

[4] X.-J. Pei, L. Zhu, S.-H. Cui et al., "Liquefaction characteristics of interlayer dislocation zone of Daguangbao landslide and its start-up cause," *Rock and Soil Mechanics*, vol. 40, no. 3, pp. 1085–1096, 2019.

[5] Q. Xu, X. Fan, R. Huang et al., "A catastrophic rockslide-debris flow in Wulong, Chongqing, China in 2009: background, characterization, and causes," *Landslides*, vol. 7, no. 1, pp. 75–87, 2010.

[6] B. Xu, C. Yan, and S. Xu, "Analysis of the bedding landslide due to the presence of the weak intercalated layer in the limestone," *Environmental Earth Sciences*, vol. 70, no. 6, pp. 2817–2825, 2013.

[7] G. Wu and L. Zhang, "Studying unloading failure characteristics of a rock mass using the disturbed state concept," *International Journal of Rock Mechanics and Mining Sciences*, vol. 41, pp. 419–425, 2004.

[8] Z. Yang, X. Fan, Y. Yang et al., "Deformation patterns and failure mechanism of high and steep stratified rock slopes with upper steep and lower gentle style induced by step-by-step excavations," *Environmental Earth Sciences*, vol. 81, no. 8, Article ID 229, 2022.

[9] H. Lan, C. D. Martin, and J. C. Andersson, "Evolution of in situ rock mass damage induced by mechanical–thermal loading," *Rock Mechanics and Rock Engineering*, vol. 46, no. 1, pp. 153–168, 2013.

[10] S. Zhang, X. Pei, S. Wang, R. Huang, and X. Zhang, "Centrifuge model testing of loess landslides induced by excavation in Northwest China," *International Journal of Geomechanics*, vol. 20, no. 4, Article ID 20, 2020.

[11] Y. H. Wang, "Analysis of engineering landslides controlled by muddy inclusions in layered rock massifs," in *Proceedings of the Fifth National Conference on Engineering Geology*, pp. 103–106, Seismological Press, Beijing, 1996.

[12] P.-D. Su, Y.-H. Tang, Y.-C. Ma, S.-F. Su, R. Zhang, and Z.-K. Qi, "Progressive failure of slope with weak interlayer strain softening," *Journal of Yangtze River Scientific Research Institute*, vol. 39, no. 6, pp. 69–75, 2022.

[13] C. L. Mu, X. J. Pei, R. Wang, and C. Wang, "Analysis on deformation characteristics of a cutting high bedding rock slope with multiple weak layers based on physical model tests," *The Chinese Journal of Geological Hazard and Control*, vol. 33, no. 3, pp. 61–67, 2022.

[14] S. Chen, M. Xiao, and J. Chen, "Failure process and stability analysis of rock blocks in a large underground excavation based on a numerical method," *Mathematical Problems in Engineering*, vol. 2020, Article ID 4280428, 12 pages, 2020.

[15] H. L. Liu, L. C. Li, S. H. Li, and W. M. Yang, "The time-dependent failure mechanism of rocks and associated application in slope engineering: an explanation based on numerical investigation," *Mathematical Problems in Engineering*, vol. 2020, Article ID 1680265, 19 pages, 2020.

[16] T. Chen, C. Zhao, and Y. F. Wu, "Numerical simulation of excavation and support for highway slope with weak intercalated layers," *Journal of Chengdu Technological University*, vol. 17, no. 4, pp. 60–63, 2014.

[17] Y. F. Yun, F. T. Fang, and G. L. Guo, "Numerical simulation of excavation and support of slope with weak intercalation," *Journal of Shanxi University of Technology (Natural Science Edition)*, vol. 34, no. 6, pp. 31–35, 2018.

[18] H. Fan, S. R. Xiao, R. Q. Wei, and L. Zhang, "Analysis of the influence of weak interlayer on the stability of the mine slope," *Journal of China Three Gorges University (Natural Sciences)*, vol. 44, no. 1, pp. 54–59, 2022.

[19] J. L. Chai, *The Stability Analysis of Rock Slope with Weak Interlayer under the Unloading Influence*, Qingdao University of Technology, Qingdao, China, 2016.

[20] D. Xue, T. Li, S. Zhang, C. Ma, M. Gao, and J. Liu, "Failure mechanism and stabilization of a basalt rock slide with weak layers," *Engineering Geology*, vol. 233, pp. 213–224, 2018.

[21] H. Bao, F. Wu, P. Xi et al., "A new method for assessing slope unloading zones based on unloading strain," *Environmental Earth Sciences*, vol. 79, Article ID 350, 2020.

[22] H. Bao, K. Zhang, C. Yan, H. Lan, F. Wu, and H. Zheng, "Excavation damaged zone division and time-dependency deformation prediction: a case study of excavated rock mass at Xiaowan hydropower station," *Engineering Geology*, vol. 272, Article ID 105668, 2020.

[23] L. Y. Zhang, Y. R. Zheng, S. Y. Zhao, and W. M. Shi, "The feasibility study of strength-reduction method with FEM for calculating safety factors of soil slope stability," *Journal of Hydraulic Engineering*, no. 1, pp. 21–27, 2003.

[24] P. C. Qiu, Y. K. Long, and J. M. Zhang, "Research on deformation failure mechanism and stability of bedding cataclastic rock slope containing multi-muddy interlayers," *Applied Sciences*, vol. 13, no. 14, Article ID 8459, 2023.

[25] S. R. Zhang, T. Y. Tao, C. Wang, and K. Wang, "Three-dimensional stability analysis of dam abutment high slope dynamic behaviors considering rock mass unloading," *Chinese Journal of Rock Mechanics and Engineering*, vol. 26, pp. 3515–3521, 2007.

[26] Z. R. Zhao, W. L. Liu, and Z. Q. Wang, *Investigation Report on Side (Slip) Slope Management Project for Yuxi City Domestic Waste Incineration Power Generation Project*, Kunming Prospecting Design Institute of China Nonferrous Metals Industry Co., Ltd., Kunming, China, 2019.

[27] J. B. Liu, "Comparative study of two methods to inverse the elastic modulus of concrete masonry gravity dam," *Pearl River*, no. 4, pp. 59–62, 2014.

[28] X. H. Song, T. Bao, and H. H. Yan, "Simulation analysis of instability failure of stone masonry weight balanced retaining wall," *Subgrade Engineering*, no. 3, pp. 127–131, 2020.
[29] J. L. Li, *Unloading Rock Mass Mechanics*, China Water & Power Press, Beijing, 1999.
[30] H. L. Hu, *Stability Parameter Sensitivity Analysis and Research on Excavation and Unloading Rock Mechanics Parameters of Rock Slopes*, China Three Gorges University, Yichang, China, 2009.
[31] Z. D. Chen, *Design of Highway Retaining Walls*, China Communication Press, Beijing, 2000.